Fermilab

Measuring the Mean Free Path of HI Ionizing Photons at $3.2 \leq z \leq 4.6$ with DESI Y1 Quasars

Measuring the Mean Free Path of H I Ionizing Photons at $3.2 \leq z \leq 4.6$ with DESI Y1 Quasars

Anning Gao [iD],[1] Jason X. Prochaska [iD],[2,3,4] Zheng Cai [iD],[1] Siwei Zou [iD],[5,1] Cheng Zhao [iD],[1] Zechang Sun [iD],[1]
S. Ahlen [iD],[6] D. Bianchi [iD],[7] D. Brooks,[8] T. Claybaugh,[9] A. de la Macorra [iD],[10] Arjun Dey [iD],[11] P. Doel,[8]
J. E. Forero-Romero [iD],[12,13] E. Gaztañaga,[14,15] S. Gontcho A Gontcho [iD],[9] G. Gutierrez,[16] K. Honscheid,[17,18]
S. Juneau,[11] A. Kremin [iD],[9] P. Martini,[19,18] A. Meisner [iD],[11] R. Miquel,[20,21] J. Moustakas [iD],[22]
A. Muñoz-Gutiérrez,[10] J. A. Newman,[23] I. Pérez-Ràfols [iD],[24] G. Rossi,[25] E. Sanchez [iD],[26] M. Schubnell,[27]
D. Sprayberry,[11] G. Tarlé [iD],[28] B. A. Weaver,[11] and H. Zou [iD][29]

[1] Department of Astronomy, Tsinghua University, Beijing 100084, China
[2] Department of Astronomy and Astrophysics, UCO/Lick Observatory, University of California, 1156 High Street, Santa Cruz, CA 95064, USA
[3] Kavli Institute for the Physics and Mathematics of the Universe (Kavli IPMU), 5-1-5 Kashiwanoha, Kashiwa 277-8583, Japan
[4] Division of Science, National Astronomical Observatory of Japan, 2-21-1 Osawa, Mitaka, Tokyo 181-8588, Japan
[5] Chinese Academy of Sciences South America Center for Astronomy, National Astronomical Observatories, CAS, Beijing 100101, China
[6] Physics Dept., Boston University, 590 Commonwealth Avenue, Boston, MA 02215, USA
[7] Dipartimento di Fisica "Aldo Pontremoli", Università degli Studi di Milano, Via Celoria 16, I-20133 Milano, Italy
[8] Department of Physics & Astronomy, University College London, Gower Street, London, WC1E 6BT, UK
[9] Lawrence Berkeley National Laboratory, 1 Cyclotron Road, Berkeley, CA 94720, USA
[10] Instituto de Física, Universidad Nacional Autónoma de México, Cd. de México C.P. 04510, México
[11] NSF NOIRLab, 950 N. Cherry Ave., Tucson, AZ 85719, USA
[12] Departamento de Física, Universidad de los Andes, Cra. 1 No. 18A-10, Edificio Ip, CP 111711, Bogotá, Colombia
[13] Observatorio Astronómico, Universidad de los Andes, Cra. 1 No. 18A-10, Edificio H, CP 111711 Bogotá, Colombia
[14] Institute of Cosmology and Gravitation, University of Portsmouth, Dennis Sciama Building, Portsmouth, PO1 3FX, UK
[15] Institut d'Estudis Espacials de Catalunya (IEEC), 08034 Barcelona, Spain
[16] Fermi National Accelerator Laboratory, PO Box 500, Batavia, IL 60510, USA
[17] Department of Physics, The Ohio State University, 191 West Woodruff Avenue, Columbus, OH 43210, USA
[18] Center for Cosmology and AstroParticle Physics, The Ohio State University, 191 West Woodruff Avenue, Columbus, OH 43210, USA
[19] Department of Astronomy, The Ohio State University, 4055 McPherson Laboratory, 140 W 18th Avenue, Columbus, OH 43210, USA
[20] Institut de Física d'Altes Energies (IFAE), The Barcelona Institute of Science and Technology, Campus UAB, 08193 Bellaterra Barcelona, Spain
[21] Institució Catalana de Recerca i Estudis Avançats, Passeig de Lluís Companys, 23, 08010 Barcelona, Spain
[22] Department of Physics and Astronomy, Siena College, 515 Loudon Road, Loudonville, NY 12211, USA
[23] Department of Physics & Astronomy and Pittsburgh Particle Physics, Astrophysics, and Cosmology Center (PITT PACC), University of Pittsburgh, 3941 O'Hara Street, Pittsburgh, PA 15260, USA
[24] Departament de Física, EEBE, Universitat Politècnica de Catalunya, c/Eduard Maristany 10, 08930 Barcelona, Spain
[25] Department of Physics and Astronomy, Sejong University, Seoul, 143-747, Korea
[26] Barcelona-Madrid RPG - Centro de Investigaciones Energéticas, Medioambientales y Tecnológicas
[27] Department of Physics, University of Michigan, Ann Arbor, MI 48109, USA
[28] University of Michigan, Ann Arbor, MI 48109, USA
[29] National Astronomical Observatories, Chinese Academy of Sciences, A20 Datun Rd., Chaoyang District, Beijing, 100012, P.R. China

ABSTRACT

The mean free path of ionizing photons for neutral hydrogen ($\lambda_{\mathrm{mfp}}^{912}$) is a crucial quantity in modelling the ionization state of the intergalactic medium (IGM) and the extragalactic ultraviolet background (EUVB), and is widely used in hydrodynamical simulations of galaxies and reionization. We construct the largest quasar spectrum dataset to date – 12,595 S/N > 3 spectra – using the Y1 observation of Dark Energy Spectroscopic Instrument (DESI) to make the most precise model-independent measurement of the mean free path at $3.2 \leq z \leq 4.6$. By stacking the spectra in 17 redshift bins and modelling the Lyman continuum profile, we get a redshift evolution $\lambda_{\mathrm{mfp}}^{912} \propto (1+z)^{-4.27}$ at $2 \leq z \leq 5$, which

is much shallower than previous estimates. We then explore the sources of systematic bias, including the choice of intrinsic quasar continuum, the consideration of Lyman series opacity and Lyman limit opacity evolution and the definition of $\lambda_{\mathrm{mfp}}^{912}$. Combining our results with estimates of $\lambda_{\mathrm{mfp}}^{912}$ at higher redshifts, we conclude at high confidence that the evolution in $\lambda_{\mathrm{mfp}}^{912}$ steepens at $z \approx 5$. We interpret this inflection as the transition from the end of HI reionization to a fully ionized plasma which characterizes the intergalactic medium of the past ~ 10 billion years.

1. INTRODUCTION

The bulk of gas existing in the vast space between galaxies, commonly referred to as intergalactic medium (IGM), is highly ionized after the epoch of reionization (Gunn & Peterson 1965). Ionizing photons from quasars and star-forming galaxies, which generate the extragalactic ultraviolet background (EUVB), play a crucial role in ionizing the neutral hydrogen in IGM (Fan et al. 2006; Faucher-Giguère et al. 2008a; Cowie et al. 2009; Becker & Bolton 2013; Madau & Haardt 2015; Jiang et al. 2022). Hydrodynamical simulations also rely on the EUVB, as they provide an important source of heating and photoionization to the ionized plasma (e.g. Oppenheimer & Davé 2006; Bolton & Haehnelt 2007; Somerville & Davé 2015; Schaye et al. 2015; Davé et al. 2019; Villasenor et al. 2021).

To estimate EUVB, except the photon emissivity of quasars and galaxies, it is necessary to measure the HI Lyman limit opacity, frequently described by the mean free path of ionizing photons (Haardt & Madau 1996, 2012). Previous studies have used various methods to measure the mean free path. Observations of high-redshift quasar spectra showed the existence of Lyα forest, which is composed of a series of HI absorbers at the blueward of restframe Lyα emission line that follows the underlying matter distribution (Rauch 1998). The mean free path can be calculated by integrating the distribution of column densities of these absorbers and its redshift evolution $f(N_{\mathrm{H\,I}}, z) = \partial^2 n/(\partial N_{\mathrm{H\,I}} \partial z)$ (e.g. Meiksin & Madau 1993; Faucher-Giguère et al. 2009; Prochaska et al. 2010; Rudie et al. 2013). However, this method relies on the assumption of the placement randomness of absorbers, thus suffering from the uncertainties from line blending and absorber clustering (Prochaska et al. 2014).

Another method that directly measures the mean free path exploits the composite of a large sample of quasar spectra, which is proved to significantly reduce the uncertainties (Prochaska et al. 2009). Using this method, the mean free path has been measured at $2 \lesssim z \lesssim 5$ with spectra from both ground-based and space-based telescopes, yielding $\lambda_{\mathrm{mfp}}^{912} \propto (1+z)^{-5.4}$ (Prochaska et al. 2009; O'Meara et al. 2013; Fumagalli et al. 2013; Worseck et al. 2014), while other measurements show a slightly shorter $\lambda_{\mathrm{mfp}}^{912}$ at $z \sim 2.2$ (Lusso et al. 2018).

Recently the mean free path has been used to probe the end of reionization by taking into account the quasar proximity effect, which suggests a much steeper evolution at $z \gtrsim 5$ indicative of a late-ending reionization model (Cain et al. 2021; Becker et al. 2021; Zhu et al. 2023; Gaikwad et al. 2023; Davies et al. 2024; Roth et al. 2024). The mean free path can also be constrained from the individual quasar sightlines, e.g. by comparing the flux ratios between the blueward and the redward of the Lyman limit (Romano et al. 2019) or finding Lyman limit systems (LLS) closest to the emitting quasar using the absorption of the first 6 transitions of Lyman series (Bosman 2021).

The Dark Energy Spectroscopic Instrument (DESI; DESI Collaboration et al. 2016a,b) started its main survey of the first year in May 2021 and finished in June 2022. As a Stage-IV spectroscopic survey, DESI observed approximately 1.4 million quasars during its first year (Y1) main survey (DESI Collaboration et al. 2025). This achievement has resulted in today's largest quasar spectroscopic catalog, and enables today's most precise measurements of dark energy and large scale structures (DESI Collaboration et al. 2024a,b,c). The large sample from DESI provides a great opportunity to measure the mean free path more precisely. In this paper, we use DESI Y1 quasar spectra to measure the mean free path at $3.2 \leq z \leq 4.6$ employing the updated statistical methods of Prochaska et al. (2009) (hereafter P09). With the sample size increased by an order-of-magnitude compared with Sloan Digital Sky Survey (SDSS) I and SDSS-II (Schneider et al. 2010, used in P09), we obtain the measurements with the uncertainty $\sim 70\%$ lower than previous work. Our updated values of mean free path show a smoother redshift evolution compared with Worseck et al. (2014) (hereafter W14), and can be useful in establishing a more precise model of EUVB.

The rest of the paper is organized as follows. In Section 2 we will briefly introduce the characteristics of DESI spectra and discuss how we selected the quasar samples from its Y1 dataset. In Section 3 we will describe our methodology in detail, including the stacking of spectra, the theoretical model and the fitting method. We will present our results in Section 4 and We discuss how our refined results of mean free path

could impact the modelling of other aspects in astrophysics and cosmology, particularly the modelling of reionization in Section 5 and summarize our conclusions in Section 6. Unless otherwise specified, a flat ΛCDM cosmology is adopted, with $\Omega_m = 0.3$, $\Omega_\Lambda = 0.7$ and $H_0 = 70 \, \mathrm{km \, s^{-1} \, Mpc^{-1}}$, and all the distances are proper distances unless stated otherwise.

2. DATA

In this section, we first summarize the properties of DESI quasars and their spectra, and discuss the potential bias that could affect our result. Then we introduce our criteria for selecting our quasar sample from DESI.

2.1. *The DESI Quasar Sample*

DESI was installed on the 4-meter Mayall telescope at Kitt Peak, Arizona, along with 5,000 fibers and fiber-positioners. It employs three spectrographs to obtain spectra simultaneously, commonly referred to as "b"(360-593 nm), "r"(560-772 nm) and "z"(747-980 nm), with the FWHM resolution $\lambda/\Delta\lambda$ ranging from 2000 (blue end) to 5500 (red end). (DESI Collaboration et al. 2022). The observation is divided into dark, bright and backup programs according to the observing condition, and quasars were observed in the dark program with an effective exposure time of $\sim 1000 \, \mathrm{s}$ (Schlafly et al. 2023). CCD images are then processed to give a common $0.8 \, \text{Å/pixel}$ wavelength grid for all spectra (Guy et al. 2023).

A complete and not biased quasar sample is crucial for our analysis. Here we briefly summarize the main procedure and results of DESI quasar target selection and validation (Chaussidon et al. 2023). DESI incorporates the optical photometry data of grz bands from the Beijing-Arizona Sky Survey, the Mayall z-band Legacy Survey (MzLS) and the Dark Energy Camera Legacy Survey (DECaLS) and the near infrared photometry data of W1 and W2 bands from the WISE satellite (Dey et al. 2019), based on which a random forest algorithm is designed to select quasars in the magnitude range $16.5 < r < 23$. In parallel, other criteria (e.g. source morphology) were tested during the Survey Validation (SV; Alexander et al. 2023; DESI Collaboration et al. 2024d) to better select faint quasars and high-z quasars. The final quasar catalog is constructed after a template-fitting algorithm REDROCK (Anand et al. 2024; Bailey et al. 2024), a broad Mg II line finder and a deep convolutional neural network QuasarNet (Busca & Balland 2018) are successively applied on the observed spectra, with the redshift determined at the same time. The overall procedure finally achieves a >99% efficiency, a >98% purity, and an approximately $60 \, \mathrm{deg^{-2}}$ target density for $z > 2.1$ quasars (Chaussidon et al. 2023).

Despite of the excellent performance of DESI target selection pipeline, we stress that there may still be possible biases that could affect our measurement. One of the main biases could be the quasar color selection. As discussed in Worseck & Prochaska (2011), the color selection criterion of SDSS selects $3 \lesssim z \lesssim 3.5$ quasars that are systematically redder on $u - g$ color and have more intervening LLSs, which is due to the difficulty of distinguishing quasars from stars in this redshift range and causes the underestimation of the mean free path measured in P09. As we can see in Figure 1, stellar contamination still exists in DESI data at $3 \lesssim z \lesssim 3.5$ and there still lacks a detailed study of DESI quasar selection bias. However, in this work we treat the DESI sample as unbiased, since the infrared observations, the more advanced random forest algorithm and the color-independent quasar variability are incorporated in DESI main selection (Chaussidon et al. 2023). We still remain cautious for the potential biases, and careful examination is needed in future studies.

2.2. *Sample Selection*

We select our sample of 12,595 quasars from the main survey, dark program of DESI Y1 observation. In particular, we apply the following selection rules:

1. $3.2 \leq z \leq 4.6$, where the redshift is determined by REDROCK. This range is set by our measuring method. As we will see in Section 3, our method requires the stacking of spectra and the fitting of the spectrum below the restframe Lyman limit ($912 \, \text{Å}$). There is only a small number of $z > 4.6$ quasars that meet the other rules, which was deemed insufficient for stacking. Below $z < 3.2$, quasars have a very short spectrum below the restframe Lyman limit which is too little for robust fitting.

2. ZWARN=0 to avoid problematic redshift determination, where ZWARN is one of the outputs of REDROCK (Guy et al. 2023; DESI Collaboration et al. 2024e,d).

3. Avoid broad absorption line (BAL) systems. Specifically, we require that the intrinsic absorption index (AI; Hall et al. 2002) and the balnicity index (BI; Weymann et al. 1991) of C IV and Si IV are all zero, which are derived from the future Data Release 1 BAL catalog and calculated using the methods in Filbert et al. (2024).

4. The signal-to-noise-ratio (S/N) estimated at restframe 1450-1470 Å is larger than 3. Following P09, this rule is meant to decrease the variation in the
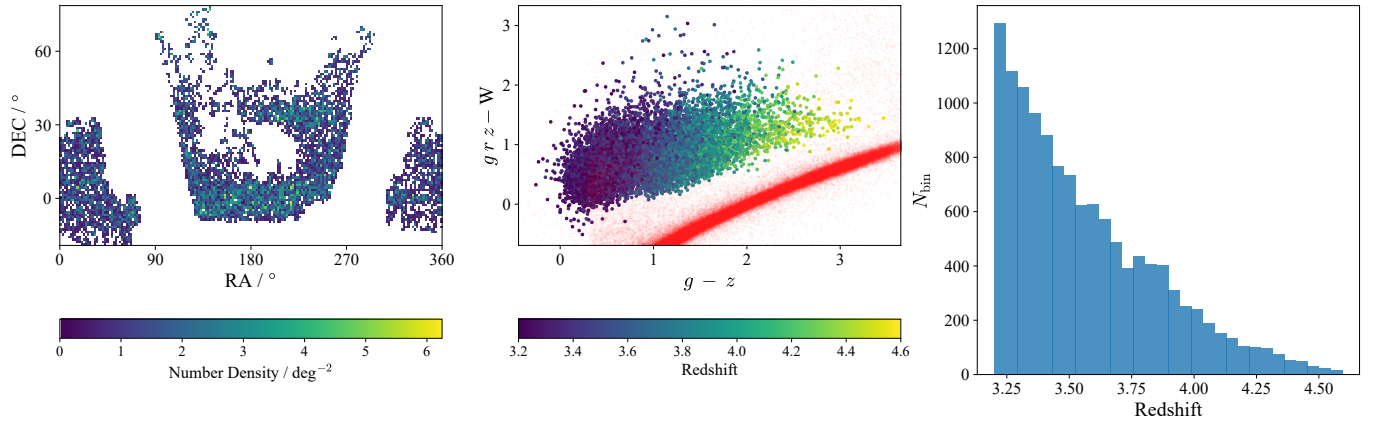
Figure 1. Parameter distributions of the DESI quasar sample analyzed here. Left panel: The distribution of angular positions, showing a roughly uniform distribution across the survey area. Middle panel: The distribution of quasar magnitude and color, coloring with redshift. The x-axis is the $g - z$ color, and the y-axis is the color defined in Chaussidon et al. (2023) that combines the optical grz bands and the infrared W1 and W2 bands. To better illustrate the stellar contaminants, we use red points to represent the stellar color from the Early Data Realease of DESI Milky Way Survey (Koposov et al. 2024), filtered with RVS_WARN=0 and RR_SPECTYPE=0 as well as PRIMARY=True (see their Section 5.1). Right panel: The distribution of redshift. $N_{\rm bin}$ means the number of quasar sightlines within the redshift bin.

stacking spectra. We also construct other samples for S/N cut of 5, 7 and 10 to perform our following fitting procedures, and our results are shown to be insensitive to the selection of S/N cut.

After selection, the official pipeline[1] is used to combine the three cameras. The galactic extinction is corrected both for flux and error to maintain S/N, using the extinction function in Cardelli et al. (1989) ($R_V = 3.1$) and the dust extinction map in Schlegel et al. (1998). Distributions of angular location, color and redshift of our sample are summarized in Figure 1.

3. METHODOLOGY

In this section, we detail our technique of mean free path measurements. Following W14, we define the mean free path as the mean distance that the ionizing photons will travel before suffering an $1/e$ amount of attenuation, where e is the base of natural logarithms.

3.1. *Stacking*

Since mean free path is a statistical quantity, the stacking of spectra is important to our analysis. Here we follow the procedures in O'Meara et al. (2013). We divide the quasar sample into 17 redshift bins, with 1,000 or 500 quasars in each bin, except that the last one has 95 quasars. The reason why the higher redshift bins have only 500 quasars instead of 1000 is that we want to keep a balance between the redshift uncertainty and the $\lambda_{\rm mfp}^{912}$ uncertainty. The detailed information of each bin is

shown in Table 1. For each redshift bin, the spectra are shifted to the quasar's restframe and normalized with the median flux at 1450-1470 Å. Since the wavelength grid size after redshift-shifting is $0.8\,\text{Å}/(1+z_{\rm qso}) < 0.2\,\text{Å}$ for all the spectra, where $z_{\rm qso}$ is the quasar redshift, we choose a 0.5 Å/pixel wavelength grid for stacking, ensuring that for each pixel in the stacked spectra, there is at least one pixel from every original spectra that can be stacked into that pixel. The stacked flux is chosen to be the mean of stacked pixels. The stacked flux uncertainty is calculated as:

$$\sigma_{\rm stacked} = \frac{1}{n}\sqrt{\sigma_1^2 + \sigma_2^2 + \cdots + \sigma_n^2} \qquad (1)$$

i.e. we treat the flux as independent Gaussian distribution (For the independence, see Guy et al. 2023, Section 4.5). We give every sightline an equal stacking weight, as each sightline represents a spatial direction that should be treated equally. All the pixels with a non-zero maskbit are neglected during stacking. We stress that we do not use the inverse variance weighting. Although it would of course reduce the variance of our composite spectra, it would also introduce an unwanted prior that gives high S/N sightlines more weights and may bias our result. Figure 2 shows several examples of our stacked spectra.

To estimate the sample variance and the uncertainties introduced by redshift error, we use the bootstrap technique. For each redshift bin, a random sample is generated from the quasars of this bin, allowing for duplication. Then each spectrum's redshift is allowed for a random Gaussian change, with 0 mean and the standard deviation of the redshift error equivalent to

---

[1] https://github.com/desihub/desispec
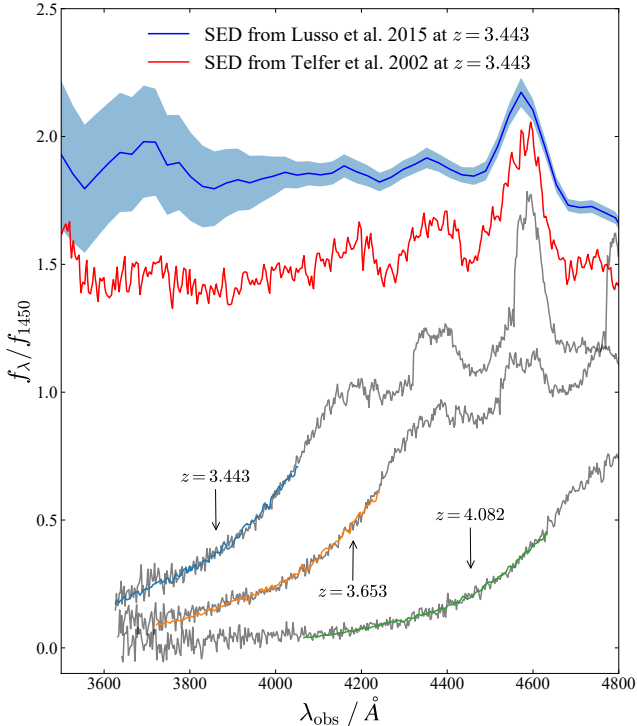
Figure 2. Examples of our stacked spectra. The grey spectra are the $z_{\mathrm{median}} = 3.443$ (left), $z_{\mathrm{median}} = 3.653$ (middle) and $z_{\mathrm{median}} = 4.083$ (right) stacks, shifted to the observation frame. Overplotted are the best fitted model. The red spectrum is the T02 SED, and the blue spectrum at the top is the L15 SED, with the lighter blue region indicating the 1σ confidence region. The two SEDs are both shifted to $z_{\mathrm{qso}} = 3.443$ to be comparable with the leftmost stack. All the five spectra are normalized at 1450Å. Overplotted on the DESI stacked spectra are the best-fitting models using T02 SED. An illustration of the composite spectra and SED templates redward of Lymanα is shown in Appendix A.

350 km/s, which is inspired by the visual inspection results of DESI quasars (Alexander et al. 2023). Those spectra are stacked using the procedures described before and shares the same wavelength grid with the previous stacks. This process is performed 1,000 times, and 1,000 different stacks are generated, which are then used to perform Markov Chain Monte Carlo (MCMC) analysis, as described in Section 3.3.

3.2. Modelling

We use the technique in P09 to analyze the stacked spectrum at $\lambda < 912$ Å, which is widely used in previous mean free path measurements (Fumagalli et al. 2013; O'Meara et al. 2013; W14; Lusso et al. 2018). This portion of the spectrum is modelled to be the intrinsic spectral energy distribution (SED) attenuated by Lyman series effective optical depth, $\tau_{\lambda_r}^{\mathrm{LyS}}$, which is caused when the photons with restframe wavelength λ_r is redshifted

to a specific Lyman series line (Lyα, Lyβ, etc.), and Lyman continuum effective optical depth, $\tau_{\lambda_r}^{\mathrm{LyC}}$, which is caused when the photon's wavelength is shorter than 912 Å so that it can ionize H I atoms. We can write down the explicit expression:

$$f_{\lambda_r} = f_{\lambda_r}^{\mathrm{SED}} \exp\left(-\tau_{\lambda_r}^{\mathrm{LyS}}\right) \exp\left(-\tau_{\lambda_r}^{\mathrm{LyC}}\right) \qquad (2)$$

where f_{λ_r} is the observed composite spectrum and $f_{\lambda_r}^{\mathrm{SED}}$ is the intrinsic quasar SED. The three parts of Equation 2 are modelled as follows, following O'Meara et al. (2013), W14 and Lusso et al. (2018): (i) The quasar SED is assumed to be a template modified by a power law:

$$f_{\lambda_r}^{\mathrm{SED}} = f_0 f_{\lambda_r}^{\mathrm{tem}} \left(\frac{\lambda_r}{912\,\text{Å}}\right)^{-\alpha} \qquad (3)$$

where f_0 is a normalization factor accounting for the continuum uncertainty and $f_{\lambda_r}^{\mathrm{tem}}$ is the SED template. Telfer et al. (2002) (hereafter T02) and Lusso et al. (2015) (hereafter L15) both stacked quasar spectra from *Hubble Space Telescope* (*HST*) and obtained average SEDs differing by $\sim 30\%$ at Lyman continuum. For comparison, we use the SED template from both two composites and show the results in Table 1. The base of the power law modification is chosen to be 912Å instead of the widely used 1450Å because we only want this modification to impact the slope of SED at Lyman continuum, and 1450Å base would introduce an additional overall normalization at Lyman continuum that could be degenerate with f_0.

(ii) The Lyman series optical depth is described by a power law:

$$\tau_{\lambda_r}^{\mathrm{LyS}} = \tau_0^{\mathrm{LyS}} \left(\frac{1 + z_{912}}{1 + z_{\mathrm{qso}}}\right)^{\gamma_\tau} \qquad (4)$$

where z_{qso} is the quasar redshift (represented by the median redshift of stacked spectra) and z_{912} is defined as:

$$1 + z_{912} = \frac{\lambda_r}{912\,\text{Å}}(1 + z_{\mathrm{qso}}) \qquad (5)$$

i.e. z_{912} represents the redshift at which the λ_r photon is shifted to 912 Å. This power law is inspired by Prochaska et al. (2014) and the index γ_τ is chosen to be 3 for all redshift bins, which are justified in Appendix B. In practice, the coefficient τ_0^{LyS} is determined by the absorption at restframe 912 Å. We stress that this term is the key difference between our measurements and the analysis in P09, where the authors only considered the Lyman continuum opacity and measured a mean free path systematically higher than ours. A detailed explanation is given in Section 4.

(iii) The Lyman limit optical depth is described by (P09; O'Meara et al. 2013):

$$\tau_{\lambda_r}^{\mathrm{LyC}} = \int \kappa \, \mathrm{d}r \qquad (6)$$

where κ is the opacity coefficient, whose redshift evolution and frequency dependence is modelled separately:

$$\begin{aligned}
\kappa =& \kappa_0 \left(\frac{1+z}{1+z_{\mathrm{qso}}} \right)^{\gamma_\kappa} \left(\frac{\nu}{\nu_{912}} \right)^{-2.75} \\
=& \kappa_0 \left(\frac{1+z}{1+z_{\mathrm{qso}}} \right)^{\gamma_\kappa} \left(\frac{1+z}{1+z_{912}} \right)^{-2.75}
\end{aligned} \qquad (7)$$

and $\mathrm{d}r$ is modelled with cosmology:

$$\frac{\mathrm{d}r}{\mathrm{d}z} = \frac{c}{H_0} \frac{1}{(1+z)\sqrt{\Omega_m(1+z)^3 + \Omega_\Lambda}} \approx \frac{c}{H_0\sqrt{\Omega_m}}(1+z)^{-2.5} \qquad (8)$$

The universe is matter-dominated at $3 < z < 5$, which justifies the last approximation in the above equation. Combining the three equations, we get:

$$\tau_{\lambda_r}^{\mathrm{LyC}} = \frac{c\kappa_0}{H_0\sqrt{\Omega_m}} \frac{(1+z_{912})^{2.75}}{(1+z_{\mathrm{qso}})^{\gamma_\kappa}} \int_{z_{912}}^{z_{\mathrm{qso}}} (1+z)^{\gamma_\kappa - 5.25} \, \mathrm{d}z \qquad (9)$$

In conclusion, there are three parameters in our model that can be fitted: the normalization factor f_0, the "effective" opacity coefficient $\kappa_{912} \equiv c\kappa_0/(H_0\sqrt{\Omega_m})$ and the evolution index γ_κ. To simplify our model, we assume $\gamma_\kappa = \alpha = 0$. This comes for two reasons: First, in our redshift range, the opacity does not evolve rapidly; Second, for the fitted wavelength range the spectrum's decline is dominated by opacity, and unless there is an extreme tilt (e.g. $|\alpha| > 0.5$), the result will not be highly influenced by it.

Finally, our definition of $\lambda_{\mathrm{mfp}}^{912}$ corresponds to a photon that has a specific emission wavelength λ_r and experiences a total Lyman limit optical depth $\tau_{\lambda_r}^{\mathrm{LyC}} = 1$, from z_{qso}, where the photon is emitted, to z_{912}, where the photon is redshifted enough to have $h\nu < 1\,\mathrm{Ryd}$. Thereby, $\lambda_{\mathrm{mfp}}^{912}$ is defined to be the physical distance between z_{qso} and z_{912} for these photons:

$$\lambda_{\mathrm{mfp}}^{912} \equiv \int c \, \mathrm{d}t = \int_{z_{912}}^{z_{\mathrm{qso}}} \frac{c \, \mathrm{d}z}{H(z)(1+z)} \qquad (10)$$

3.3. Fitting

We use the MCMC technique to estimate the posterior distribution of parameters for the composite spectra in each redshift bin. To better combine the uncertainty introduced by spectrum fluctuations, sample selection and redshift estimation, we perform MCMC analysis for each bootstrap spectrum, and combine all the posterior

with equal weights to give the final posterior. We choose the traditional form of χ^2 likelihood:

$$\chi^2 = \sum_i \left(\frac{f_i - f_i^{\mathrm{model}}}{\sigma_i} \right)^2 \qquad (11)$$

where f_i and f_i^{model} are the stacked flux and the model flux at the ith pixel and the uncertainty σ_i is defined in Equation 1 and is chosen to be the same for all the bootstrap spectra in each redshift bin to reduce the computation cost. We do not choose to represent the sample variance with the covariance matrix calculated from the bootstrap spectra, as we discovered that this would underestimate the final uncertainties of $\lambda_{\mathrm{mfp}}^{912}$, which may be probably caused by the ignorance of non-Gaussian variance. In our fiducial model, the prior is chosen to be a uniform distribution with a loose boundary $0 < f_0 < 3$, $0 < \kappa_{912} < 1000$. The lower bound of the fitted spectral region is the maximum between $800\,\text{Å}$ and the shortest wavelength that has a contribution from all of the stacked spectra.

An example of combined posterior distributions is shown in Figure 3, together with the mean free path distribution calculated from 200,000 sample points. Although the combined posterior is not strictly Gaussian, the marginal distributions of parameters and the mean free path distribution are still symmetric and can be viewed as an imperfect Gaussian shape. Therefore, the fitted value of the mean free path is chosen to be the median, and the uncertainty is chosen to be the standard deviation, which corresponds to the 68% confidence level.

4. RESULTS

Following the method, we fit the mean free path of 17 redshift bins using the stacked spectra from 12,595 quasars. All the fitted values are shown in Table 1. In Section 4.1 we explore the redshift evolution of the mean free path and discuss how our results differ from previous measurements that are listed in Appendix C. In Section 4.2 we validate our results and discuss the possible systematic uncertainties in our measurements.

4.1. Redshift Evolution of the Mean Free Path

The redshift evolution of the mean free path plays a crucial role in understanding the evolution of the thermal state of IGM and determining the content of cosmic residual neutral hydrogen at post-reionization epoch. W14 provides a comprehensive collection of $\lambda_{\mathrm{mfp}}^{912}$ and gives $\lambda_{\mathrm{mfp}}^{912} \propto (1+z)^{-5.4\pm0.4}$, which is much steeper than the speed caused by cosmic expansion only and indicates the decrease of the number and/or size of absorbers. Lusso et al. (2018), however, suggests a slower evolution
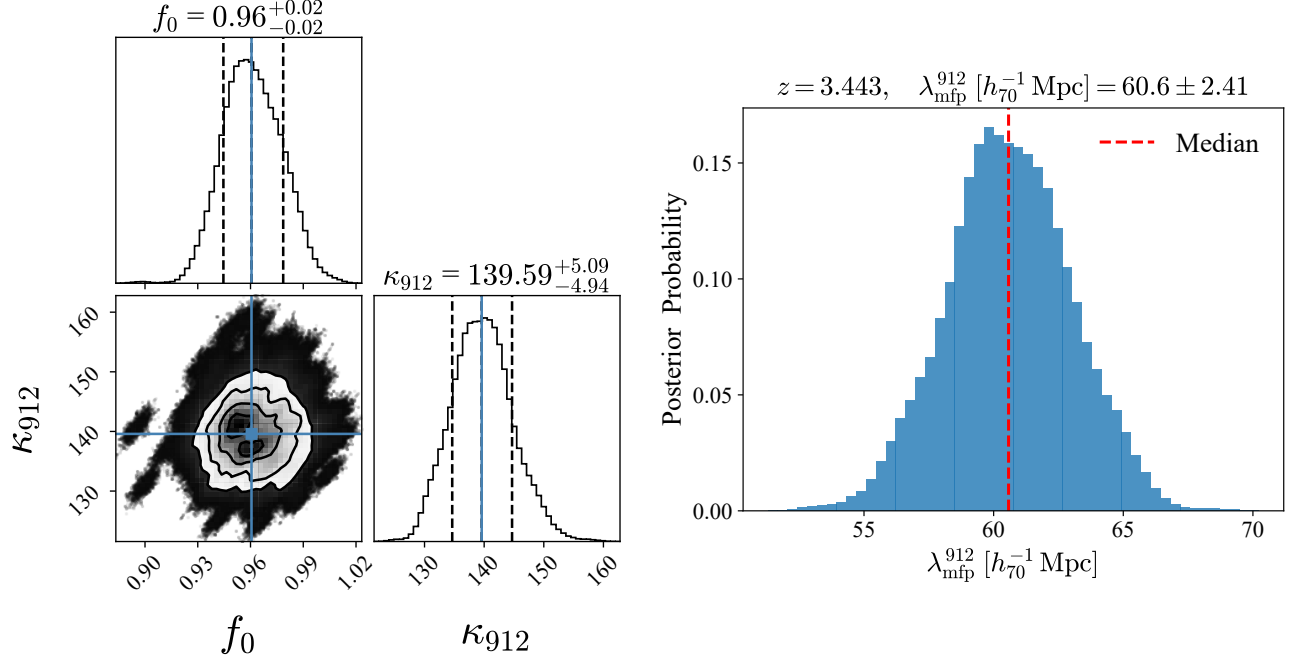
Figure 3. The combined MCMC sampling of the parameter posterior at $z_{\mathrm{median}} = 3.443$. Left panel is the 2D distribution in the parameter space. The blue lines show the median parameter values in marginal distributions that can be used as an appropriate choice for the maximum posterior estimation. The dash vertical lines denote the 16% and 84% quantiles. Right panel is the mean free path distribution calculated from the parameter posterior sample, which is mostly Gaussian-shaped.

Table 1. $\lambda_{\mathrm{mfp}}^{912}$ measurements. The unit of $\lambda_{\mathrm{mfp}}^{912}$ and A is h_{70}^{-1} Mpc.

$z_{\min}$	$z_{\max}$	z_{median}	N_{qso}	λ_r range	$\lambda_{\mathrm{mfp}}^{912}$ with T02 SED	$\lambda_{\mathrm{mfp}}^{912}$ with L15 SED
3.200	3.236	3.217	1000	857-912 Å	65.4±3.44	59.7±2.83
3.236	3.275	3.255	1000	850-912 Å	64.6±2.87	59.1±2.38
3.275	3.320	3.297	1000	842-912 Å	66.5±3.01	60.5±2.49
3.320	3.364	3.341	1000	834-912 Å	60.1±2.58	55.1±2.16
3.364	3.415	3.389	1000	825-912 Å	63.3±2.72	57.6±2.24
3.415	3.474	3.443	1000	816-912 Å	60.6±2.41	55.3±2.00
3.474	3.539	3.506	1000	805-912 Å	52.0±1.96	48.0±1.68
3.539	3.613	3.577	1000	800-912 Å	50.4±1.77	46.6±1.51
3.613	3.696	3.653	1000	800-912 Å	47.1±1.64	43.7±1.42
3.696	3.756	3.724	500	800-912 Å	43.7±2.06	40.7±1.78
3.756	3.808	3.782	500	800-912 Å	41.4±1.97	38.6±1.72
3.808	3.866	3.837	500	800-912 Å	41.3±2.11	38.5±1.85
3.866	3.931	3.896	500	800-912 Å	35.4±1.73	33.3±1.53
3.931	4.024	3.976	500	800-912 Å	35.9±1.52	33.7±1.35
4.024	4.161	4.082	500	800-912 Å	31.6±1.38	29.8±1.23
4.161	4.434	4.270	500	800-912 Å	29.5±1.15	27.8±1.03
4.434	4.600	4.489	95	800-912 Å	23.5±1.90	22.4±1.72
A					35.03 ± 0.54	32.92 ± 0.47
η					-4.03 ± 0.16	-3.84 ± 0.14

of the mean free path, $\lambda_{\mathrm{mfp}}^{912} \propto (1+z)^{-4.5\pm0.2}$, incorporating the new measurements with an updated quasar SED.

In recent years the mean free path measurements have been extended to higher redshifts, where the mean free path becomes too short to neglect the proximity effect of quasars. This effect is caused by the extra ionization of neutral hydrogen from the nearby quasars, and may bias the mean free path measurements as it is the local effects that dominates and do not reflect the opacity of the entire IGM. Becker et al. (2021) and Zhu et al. (2023) measures the mean free path at $5 \lesssim z \lesssim 6$ by considering the size of quasar proximity zone, and their measurements implies a much steeper evolution of mean free path at this redshift range.

Here we present our measurements of the mean free path using T02 SED as a function of redshift in Figure 4, together with previous measurements at $z \lesssim 5$. The T02 results are used as the fiducial results throughout the rest of this paper, as most previous measurements at similar redshifts, e.g. P09, O'Meara et al. (2013), Fumagalli et al. (2013) and W14 all used the T02 SED, and employing the same SED would help us maintain consistency and compare with these results. We also fit the two-parameter model in W14, $\lambda_{\mathrm{mfp}}^{912} = A\left[(1+z)/5\right]^{\eta}$ using MCMC and our data *only* and get $A = 35.03 \pm 0.54\,h_{70}^{-1}$ Mpc and $\eta = -4.03\pm0.16$. The two parameters fitted with our other measurements are shown at the bottom lines in Table 1.

Our measurements show several major differences comparing with the previous:

1. The uncertainties are significantly reduced due to our large sample. However, as shown in Table 1, although we use 1,000 spectra for stacking for the first 9 redshift bins and less spectra for the others, the $\lambda_{\mathrm{mfp}}^{912}$ uncertainties seem not to show corresponding smaller values for the first 9 bins, which may put a question on the necessity of employing such a large sample. We admit that it is indeed not clear if we look at the *absolute* value, but this is not the case if we look at the *relative* uncertainties. As shown in Figure 5, the first 9 bins do exhibit smaller relative uncertainties, especially if we compare the 8th and 9th points with the 10th and 11th points. The seemingly large relative uncertainties for the first 7 bins are mainly due to the shorter restframe wavelength range that we use to fit, since a shorter wavelength range gives less spectrum points available for our fitting and thus limits the constraining power.

2. The measured mean free path are systematically lower than previous estimates, especially P09. The discrepancy occurs mostly at $z \lesssim 4$, and the four points with lowest redshift in our measurements are only $\sim 75\%$ the corresponding values of the W14 power law. The discrepancy implies a systematic bias induced from either the data collection, i.e. the different target selection of DESI and SDSS, or the different fitting procedure. We explore a number of possibilities in the next subsection.

4.2. *Validations on Systematics*

To further investigate the sources of difference in Figure 4, we conduct various validations on our fitting method.

One of the most prominent sources of systematics come from the choice of quasar SED, which is highly influenced by sample selection and the method of IGM absorption correction. Parametrizing SED as $f_\nu \propto \nu^{\alpha_\nu}$, various studies show a similar spectral index α_ν in the Lyman continuum region. The quasar spectrum composite from T02 with a sample of 184 quasars and a median redshift $z \simeq 1.2$ has a spectral index $\alpha_\nu = -1.76 \pm 0.12$ at wavelength $500 \sim 1200$Å, and L15 measured a similar result $\alpha_\nu = -1.70 \pm 0.61$ at $z \simeq 2.4$. Other measurements, however, give different indices. Stevans et al. (2014) exploits the spectra of 159 active galactic nuclei (AGNs) at a median redshift $z \simeq 0.37$ observed with *HST*/COS and give $\alpha_\nu = -1.41 \pm 0.15$. Cai & Wang (2023) reports a more extreme spectral index $\alpha_\nu = -2.4\pm0.1$ after correcting the quasar selection bias. Thus it is necessary to assess the systematic bias induced by the uncertainty of spectral index. By altering the tilt factor α in Equation 3, we can change this spectral index without changing the overall level of SED. We show our measurements with different α in the left panel of Figure 5, which indicates that unless the true underlying SED exhibits an extreme spectral index and differs by more than 0.5, our measurements would not be biased by more than 5%, which is of the same scale of the statistical uncertainty, as shown in Figure 5. It is then clear that if we want to explain the discrepancy with SED slope, we would have to choose a slope that will contradict with most of previous measurements.

Another source of systematics is the overall level of SED at the Lyman continuum. Although T02 and L15 have nearly the same spectral index, their overall level differs by $\sim 30\%$ in the Lyα forest when normalized at 1450Å, as shown in Figure 2. Other SED templates have the same problem, summarized in Figure 8 of L15 and Figure 3 of Cai & Wang (2023). This problem mainly
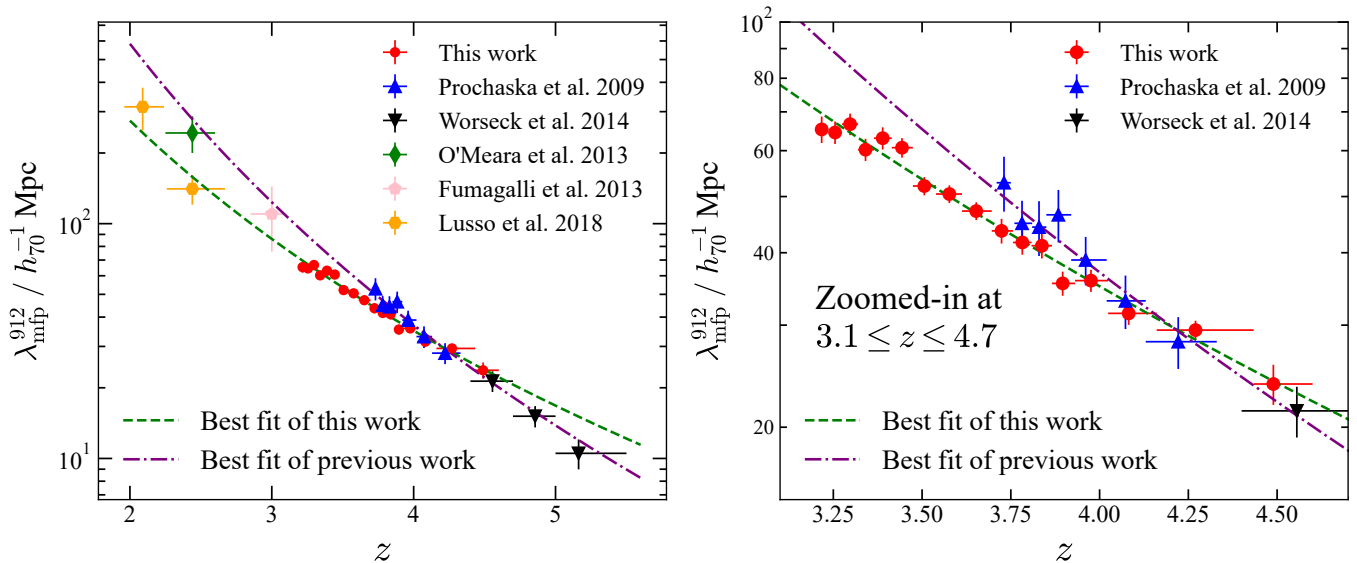
Figure 4. The measured mean free path as a function of redshift, using T02 SED. Left panel: The overall mean free path evolution at $2 \lesssim z \lesssim 5$ with data points from P09 (blue triangle-ups), Fumagalli et al. (2013) (pink pengatons), O'Meara et al. (2013) (green diamonds), W14 (black triangle-downs), Lusso et al. (2018) (orange hexagons) and our work (red circles). The violet dash-dot line and the green dash line represent the best power law fitting in W14 and our work, respectively. Right panel: The zoom-in plot at $3.1 \leq z \leq 4.7$ to better display the differences between our work and P09. Our measurements are systematically lower than the interpolation of W14 power law at $z \lesssim 4$, which is mainly due to the improper handling of Lyman series opacity evolution in P09, and our power law is roughly consistent with other previous works.

comes from the IGM absorption correction, which depends highly on the form of H I absorber distribution function $f(N_{\mathrm{H\,I}}, z)$. L15 choose the Prochaska et al. (2014) spline model, and T02 choose an empirical broken power law with parameters from various studies (see their Section 2.2). The effect of SED overall level is reflected in the estimation of τ_0^{LyS} in Equation 4, where a higher level will result in a larger τ_0^{LyS} and therefore a faster Lyman series opacity evolution. The right panel of Figure 5 shows our measurements with T02 SED multiplied by different normalization factors. The result is consistent with our thought: A higher SED will bring a faster declining of Lyman series opacity from restframe Lyman limit to shorter wavelengths, requiring the Lyman limit opacity to be higher to compensate for the total absorption. The differences between measurements using T02 and L15 can then be mostly explained by the higher overall level of L15 SED, and the remaining difference may come from the different SED fluctuations, e.g. the bump at restframe ~ 800Å in L15 SED shown in Figure 2. Combining the two uncertainties in quasar SED, we believe that the systematic bias induced by SED would not exceed $\sim 10\%$, which means the SED choice cannot entirely explain the $\sim 25\%$ discrepancy with W14.

Neglecting the Lyman limit opacity evolution when fitting, i.e. enforcing $\gamma_\kappa = 0$ in Equation 9 may also

introduce bias to our model. Most of the previous work at similar redshifts did not consider this evolution (P09, Fumagalli et al. 2013, W14, Lusso et al. 2018). O'Meara et al. (2013) fitted this parameter and found a mean value $\gamma_\kappa \simeq 0.4$ and a median value $\gamma_\kappa \simeq 0$ at $z \simeq 2$, which means $\gamma_\kappa = 0$ would be a suitable approximation. To better explore the influence of freeing γ_κ on the mean free path measurements, we use the untilted T02 SED to fit our stacked spectra with a $\gamma_\kappa > 0$ uniform prior. These measurements are shown in Table 2, together with an example combined MCMC posterior shown in Figure 6, where the results are mostly consistent with results in Table 1, except that the result of the lowest redshift in Table 2 is not physical, which we believe comes from a wavelength range that is too short to constrain γ_κ. Additionally, most γ_κ fittings also deviate from 0, which is not surprising as the mean free path also evolves quickly in these redshift. In conclusion, neglecting γ_κ would not bias our measurements, so we continue to keep $\gamma_\kappa = 0$ hereafter.

After the above considerations, we believe that the reason why our measurements are systematically lower than the power law in W14, or P09 more specifically, is the neglection of Lyman series opacity *evolution* in P09. In other words, P09 simply replace the Lyman series opacity at the blueward of 912Å with τ_0^{LyS} (Equation 4) that is estimated at exactly 912Å. By this means they
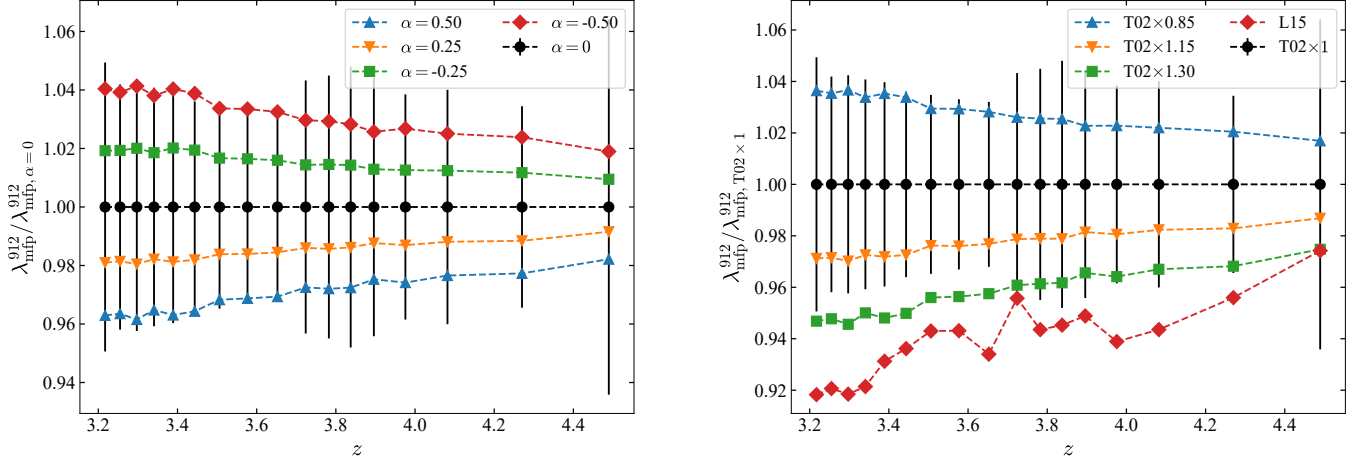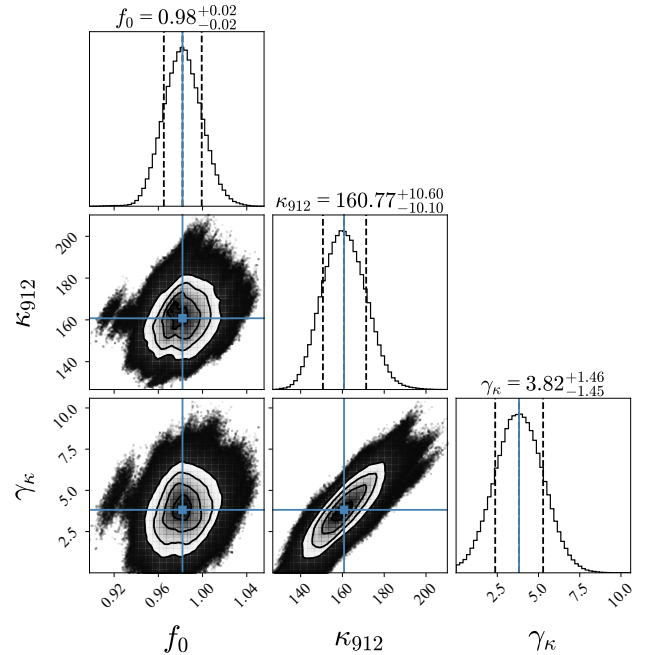
Figure 5. Measurements of different quasar SEDs compared with our default model. Left panel: Measurements when we adjust the tilt index α in Equation 3 to 0.5 (blur triangle-ups), 0.25 (orange triangle-downs), -0.25 (green squares) and -0.5 (red hexagons), which show that except for an extreme tilt ($|\alpha| \gtrsim 0.5$), our default measurements would not bias for more than 5% due to an incorrect spectral index. Right panel: Measurements with different overall normalization. The blue triangle-ups, orange triangle-downs and green squares represent the measurements when we shift the T02 SED to its 0.85, 1.15 and 1.30 times. For comparison we also draw the measurements with L15, represented by red hexagons. The difference between L15 and T02 measurements can then be explained for $\sim 70\%$ by the overall height of SED, and the remaining $\sim 30\%$ may come from the shape fluctuations.

Table 2. γ_κ and $\lambda_{\mathrm{mfp}}^{912}$ measurements when freeing γ_κ. The unit of $\lambda_{\mathrm{mfp}}^{912}$ is h_{70}^{-1} Mpc. Since we applied $\gamma_\kappa > 0$ prior, the γ_κ estimates with their posterior peaking at $\gamma_\kappa = 0$ are underlined, and their uncertainties are the 50% quantile. Other posteriors peak at nearly 50%, so the upper and lower uncertainties are chosen to be the 84% and 16% quantiles.

z_{median}	γ_κ	$\lambda_{\mathrm{mfp}}^{912}$
3.217	$11.56^{+3.79}_{-3.67}$	439.4 ± 5.88
3.255	$\underline{0.00 + 0.68}$	65.4 ± 3.10
3.297	$\underline{0.00 + 2.28}$	68.1 ± 3.45
3.341	$3.81^{+1.92}_{-1.77}$	61.0 ± 2.93
3.389	$3.07^{+1.75}_{-1.65}$	63.9 ± 3.01
3.443	$3.82^{+1.46}_{-1.45}$	60.3 ± 2.71
3.506	$2.82^{+1.16}_{-1.23}$	50.9 ± 2.14
3.577	$2.29^{+1.08}_{-1.14}$	49.2 ± 1.91
3.653	$2.93^{+1.11}_{-1.07}$	45.3 ± 1.83
3.724	$3.72^{+1.38}_{-1.45}$	41.2 ± 2.22
3.782	$2.53^{+1.45}_{-1.42}$	39.5 ± 2.17
3.837	$4.02^{+1.30}_{-1.29}$	38.1 ± 2.20
3.896	$2.22^{+1.36}_{-1.29}$	33.9 ± 1.87
3.976	$\underline{0.00 + 0.99}$	35.1 ± 1.64
4.082	$1.69^{+1.26}_{-1.12}$	30.5 ± 1.53
4.270	$\underline{0.00 + 0.50}$	29.1 ± 1.22
4.489	$\underline{0.00 + 3.25}$	22.1 ± 2.06

Figure 6. MCMC sampling of the parameter posterior at $z_{\mathrm{median}} = 3.443$ when the parameter γ_κ in Equation 4 is freed.

overestimated the Lyman series opacity, leading to an overestimation of the mean free path. To test our idea, we use exactly the same data in P09 and add the $\gamma_\tau = 3$

evolution to remeasure the mean free path, shown in Figure 7 (purple pentagons), together with the original value in P09 (blue up-triangles). Comparing the two sets of data, the neglection of the Lyman limit opacity evolution could produce a discrepancy more than 20%, implying this is a major source of the difference. How-

ever, correcting this neglection would over-correct the mean free path results and make them lower than the $\lambda_{\rm mfp}^{912} \propto (1+z)^{-4.03}$ model (Figure 7, purple pentagons v.s. green dash line), which indicates the existence of other bias.

We believe the last source of systematic bias is the definition of the mean free path. Different from ours, P09 defines $\lambda_{\rm mfp}^{912} = 1/\kappa_0$, where κ_0 is the opacity at the redshift of emission quasars (Equation 7). Theoretically, the $1/\kappa_0$ definition estimates the opacity at the light emission source, while the $\tau^{\rm LyC} = 1$ definition involves the opacity evolution along the travel of the photons, which would take the evolved lower opacity into consideration and generate a higher mean free path. Results shown in Figure 7 support this claim: measurements with $1/\kappa_0$ definition are indeed lower by $5-10\%$ than that with the $\tau^{\rm LyC} = 1$ definition (orange hexagons v.s. green down-triangles, grey squares v.s. purple pentagons). In Inoue et al. (2014), the authors also explored the difference between different definitions and came to a similar conclusion. Interestingly, the definition choice in P09 partially offsets the impact of setting $\gamma_\tau = 0$, and together they produce the $\sim 20\%$ discrepancy in P09 redshift range. Taking the two factors into consideration, our fitting pipeline reproduces the results in P09 (Figure 7, green down-triangles), which further confirms the validity of our method.

To sum up, we assess several possible sources of systematic bias in the mean free path measurements. The uncertainty of quasar SED, including its spectral index and the overall level at the Lyman continuum, would bias the mean free path results for $\sim 10\%$. Given that the precise quasar SED is still under debate, a less biased SED template is needed for future mean free path measurements. The neglecting of γ_κ do not introduce bias and is appropriate for most redshift ranges, but the different treatment of γ_τ is the key factor that causes the discrepancy in Figure 4. Different mean free path definitions would also introduce secondary bias into our model.

4.3. Revised Redshift Evolution of the Mean Free Path

Combining the direct measurements from O'Meara et al. (2013), Fumagalli et al. (2013), W14, Lusso et al. (2018), Becker et al. (2021), Zhu et al. (2023), remeasured P09 and our result using T02 SED, we suggest a broken power law parameterization of the redshift evolution of mean free path, described by:

$$\lambda_{\rm mfp}^{912} = \begin{cases} A\left(\dfrac{1+z}{1+z_0}\right)^{\eta_1}, & \text{when } z \leq z_0 \\[2ex] A\left(\dfrac{1+z}{1+z_0}\right)^{\eta_2}, & \text{when } z > z_0 \end{cases} \quad (12)$$

where A, z_0, η_1, η_2 are all free parameters. With the assumption of Gaussian uncertainty, the best parameter estimates given by MCMC posterior are $A = 16.51^{+1.85}_{-0.91}\, h_{70}^{-1}\,{\rm Mpc}$, $z_0 = 4.93^{+0.06}_{-0.12}$, $\eta_1 = -4.27^{+0.14}_{-0.12}$, $\eta_2 = -17.73^{+3.13}_{-3.52}$. Figure 8 shows the well-behaved MCMC posterior and the best fitted line that is roughly consistent with all the existing direct measurements of mean free path. Measurements in Gaikwad et al. (2023), Davies et al. (2024) and Satyavolu et al. (2024) in Figure 8 are not included in the fitting, which we will discuss in Appendix D. As the parameter posterior is not Gaussian, we choose the maximum posterior estimates, and the errorbars indicate the scaled 1σ range (e.g. if the best estimate corresponds to 40% quantile, then the lower errorbar represent the $(40 \times 16/50)\%$ quantile, and the upper errorbar is the $(1 - 60 \times 16/50)\%$ quantile). We stress that we do not correct for the different SEDs of previous works in this fitting: P09, O'Meara et al. (2013), Fumagalli et al. (2013), Worseck et al. (2014) and our results use the T02 SED, while Lusso et al. (2018), Becker et al. (2021) and Zhu et al. (2023) use the variations of L15 SED. But the fitting would not bias significantly, especially at higher redshift, as we can see that the three independent measurements from W14, Becker et al. (2021) and Zhu et al. (2023) at $z \simeq 5$ almost coincide with each other. The posterior shows a distinct double-peak feature, but estimates from the two peaks are almost identical and only differ at $z \sim z_0$, so we keep the estimate from the highest peak. We calculate the Bayesian information criterion (BIC) of our broken power law model and single power law model, defined as:

$$\text{BIC} = \chi^2 + p \ln n \quad (13)$$

where n is the number of data points, 37 in this case, and p is the number of parameters, 4 for broken power law and 2 for single power law. Note that the χ^2 here is computed among the $\lambda_{\rm mfp}^{912}$ measurements and is not the one defined in Equation 11. Results show that the broken power law model achieves BIC = 51.0, much lower than the single power law model BIC = 330.7. Our fitting shows that after correcting all the systematics, a slower evolution of mean free path after $z \simeq 5$ and a break redshift $z_0 = 4.93$ are strongly favored by the existing data.

5. DISCUSSION

5.1. Impact on the Estimation of $f(N_{\rm H\,I}, z)$

Many empirical estimates of $f(N_{\rm H\,I}, z)$ have been proposed to study the IGM opacity and provide a theoretical ingredient to calculate the EUVB. We compare the measurements in this work with the most widely used
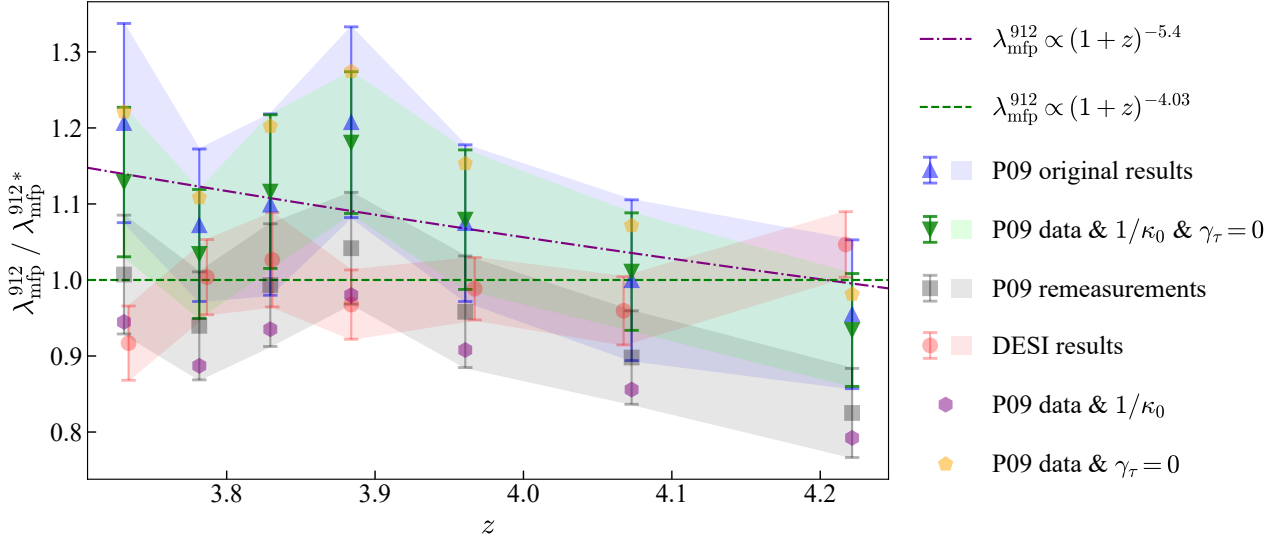
Figure 7. Comparison between different $\lambda_{\mathrm{mfp}}^{912}$ measurements. All the points and lines are normalized with our T02 power law fitting in Table 1 (denoted as $\lambda_{\mathrm{mfp}}^{912*}$ in y-axis label). The purple dash-dot line and green dash line are the W14 power law model and our $\lambda_{\mathrm{mfp}}^{912*}$ model. The blue up-triangles are the original P09 results. With the exactly same data, we use our method (grey squares), our method with $\lambda_{\mathrm{mfp}}^{912}$ definition to be $1/\kappa_0$ (purple pentagons), our method with $\gamma_\tau = 0$ (orange hexagons) and our method with both $1/\kappa_0$ definition and $\gamma_\tau = 0$ (green down-triangles) to measure $\lambda_{\mathrm{mfp}}^{912}$, respectively. Measurements with DESI stacks at the same redshift range are shown in red circles for comparison. To better illustrate the uncertainty estimates, the blue, green, grey and red dots are shaded with the same color within 1σ range, while the purple and orange dots are not. Comparing blue and green triangles, we believe that our method stays consistent with previous works in estimating both values and uncertainties. Correcting the γ_τ choice brings the P09 measurements consistent with ours (grey squares), while the $z = 4.07$ and $z = 4.22$ results deviates from our $\lambda_{\mathrm{mfp}}^{912*}$ model for more than 1σ. The different $\lambda_{\mathrm{mfp}}^{912}$ definition would generate $\sim 7\%$ bias, and neglecting γ_τ would bias the result for $\sim 20\%$.
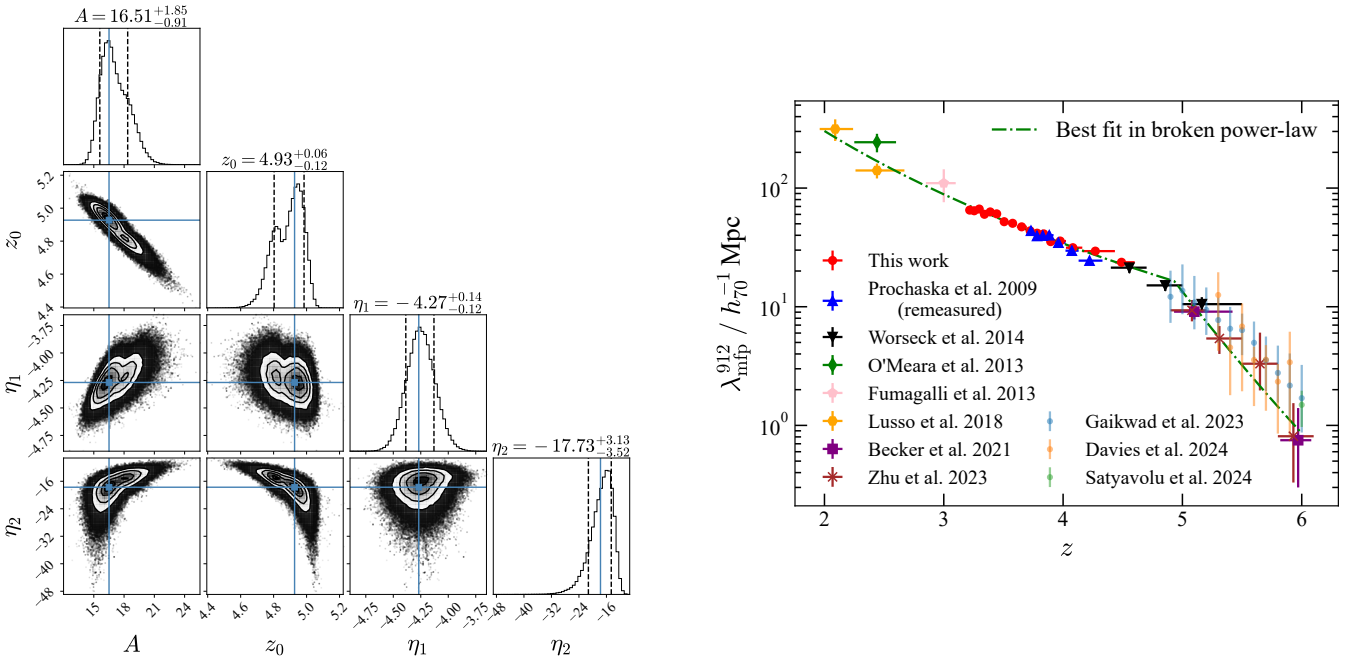
Figure 8. The broken power law fitting of the current mean free path measurements at $2 \lesssim z \lesssim 6$, using the functional form in Equation 12. Left panel: MCMC posterior of the four parameters. Right panel: The current measurements and the best fitted line. The data points in P09 (blue up-triangles) are remeasured using our pipeline, as what we do in Figure 7.

models in the literature: Haardt & Madau (2012), Inoue et al. (2014) and Puchwein et al. (2019) in Figure 9, with the z_{912} for calculating $\lambda_{\rm mfp}^{912}$ using Equation 10 defined as:

$$\tau^{\rm LyC}(z_{912}, z_{\rm qso}) = \int_0^\infty {\rm d}N_{\rm H\,I} \int_{z_{912}}^{z_{\rm qso}} f(N_{\rm H\,I}, z)$$
$$\times \left\{ 1 - \exp\left[-N_{\rm H\,I}\sigma_{\rm ph}(z) \right] \right\} {\rm d}z = 1 \tag{14}$$

where $\sigma_{\rm ph}(z)$ is the hydrogen photoionization cross section when the photon reaches redshift z. We do not include the model in Faucher-Giguère (2020), as it only differs from Puchwein et al. (2019) at low redshift. Puchwein et al. (2019) (purple line) best matches our results among the three models, while Haardt & Madau (2012) overpredict the mean free path at $z \gtrsim 3.2$ and Inoue et al. (2014) underpredict the mean free path at $z \gtrsim 4$. Nevertheless, the three models all overpredict the evolution speed implied by our measurements, illustrated with the green dash-dot line. However, the functional form in Songaila & Cowie (2010) coincides with our results. All these models are derived from the Lyα absorber statistics, which are easily biased by e.g. line blending and the clustering of absorption systems (Prochaska et al. 2010, 2014), while our method does not depend on the specific distribution of Lyα absorbers. Therefore, we encourage a further exploration of systematics and a modification of the form of $f(N_{\rm H\,I}, z)$ to better match the observations.

5.2. Implication for Reionization

The history of reionization has been studied by a large body of literature with various methods. Measurements of the optical depth for the Cosmic Microwave Background (CMB) photons set a midpoint for the reionization $z_{\rm re} = 7.82 \pm 0.71$ (Planck Collaboration et al. 2021). Although it was once believed that reionization ends at $z \simeq 6$ (e.g. McGreer et al. 2015), recent observations of high redshift quasar spectra provide evidence that reionization may extend significantly below $z \simeq 6$. The long dark gap statistics in Lyα and Lyβ forests strongly rule out a scenario with homogeneous UV background and a reionization fully completed at $z > 6$ (Zhu et al. 2021, 2022). Measurements of the Lyα effective optical depth and its fluctuations further confirm the judgement and imply an ending that could be as late as $z \simeq 5.3$ (e.g. Kulkarni et al. 2019; Yang et al. 2020; Choudhury et al. 2021; Bosman et al. 2022). The methods of dark pixels (e.g. Jin et al. 2023) and damping wings (e.g. Ďurovčíková et al. 2024; Zhu et al. 2024; Spina et al. 2024; Greig et al. 2024) are used to constrain the neu-
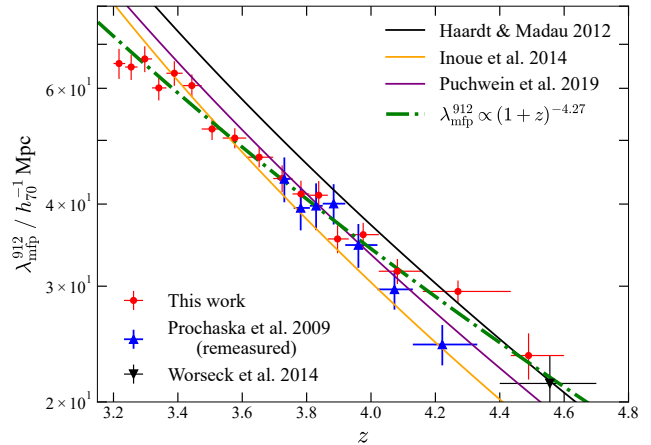
Figure 9. Comparison between our measurements and the previous $f(N_{\rm H\,I}, z)$ models. The red circles, blue up-triangles and black down-triangles are the observational measurements from our work, remeasured P09 and W14, respectively. The black, purple and yellow lines are the mean free path calculations with the Equation 10 definition, using models from Haardt & Madau (2012), Inoue et al. (2014) and Puchwein et al. (2019), respectively. The green dash-dot line represents our best broken power law fitting. All the three models in literature over-predict the evolution speed of the mean free path.

tral fraction of IGM at $5 \lesssim z \lesssim 6$ with in Lyα forest, which is a direct probe of the reionization history.

The measurements of mean free path could also be an independent probe for reionization. The mean free path is first controlled by the typical size of H II bubbles and evolves rapidly at the beginning of reionization. After the overlapping of these bubbles, the mean free path would then be controlled by the optically-thick LLS (Madau 2017; Gnedin & Madau 2022). The redshift evolution of the mean free path can therefore be separated into two stages, which is indeed shown by our broken power law fitting in Equation 12 and reproduced in numerical simulations (e.g. Cain et al. 2021; Lewis et al. 2022). However, the transition redshift $z_0 = 4.93$ that is supposed to be the time of overlapping is later than most previous estimates where the neutral fraction of IGM is constrained to be $\sim 10^{-4}$ at $z \sim 5.5$ (Fan et al. 2023). This mild tension may come from the inappropriate choice of our functional form at $z \gtrsim z_0$, but it is difficult for a more precise model to generate a more consistent transition redshift given the lack of mean free path measurements at $z \gtrsim 5$ and the large uncertainty of the existing results. Nevertheless, the measurements of Lyα effective optical depth $\tau_{\rm eff}$ may provide a supplement support for our claim. The power law evolution of $\tau_{\rm eff}$ at $2 \lesssim z \lesssim 5$ has an index $\beta \simeq 3$ (e.g. Faucher-Giguère et al. 2008b; Becker et al. 2013;

Kamble et al. 2020; Gaikwad et al. 2021; Ding et al. 2024; Turner et al. 2024), while at $z \gtrsim 5$ the evolution becomes much faster, with $\beta \simeq 10$ (e.g. Yang et al. 2020; Bosman et al. 2022). This roughly coincides with our $\lambda_{\mathrm{mfp}}^{912}$ evolution in both the break redshift and the power law index at either sides. In conclusion, the break of $\lambda_{\mathrm{mfp}}^{912}$ evolution at $z = z_0 = 4.93$ implies that reionization may end at this time, but further evidence and interpretation are still needed to better align with other independent measurements.

6. CONCLUSION

We have presented new measurements of the mean free path of neutral hydrogen ionizing photons at $3.2 \leq z \leq 4.6$. We construct the largest quasar sample containing 12,595 quasars from DESI Y1 observations. By fitting the Lyman continuum of the composite quasar spectra at 17 redshift bins, we obtain the most precise measurements to date, summarized in Table 1. Our results are systematically lower at $z \gtrsim 3$ than the previous power law interpolation in W14 and show a much shallower evolution speed. We investigate a number of possible biases, and conclude that the main reason is the neglection of the evolution of Lyman series opacity in P09. Combining with all the previous estimates, we believe that the redshift evolution can be best described by a broken power law, with the break redshift $z_0 = 4.93^{+0.06}_{-0.12}$. This evolution is slower than the predictions from most of the current $f(N_{\mathrm{H\,I}}, z)$ models, and although later than most other measurements, the power law break at $z \approx 5$ may be interpreted as the end of H I reionization. As even larger quasar samples from DESI is coming in the next few years, more precise measurements of $\lambda_{\mathrm{mfp}}^{912}$ as well as other quantities such as τ_{eff} can be conducted in the future, which we believe will provide tighter constraints on the thermal evolution of IGM at post-reionization era.

Software: astropy (Astropy Collaboration et al. 2013, 2022), numpy (van der Walt et al. 2011), matplotlib (Hunter 2007), scipy (Virtanen et al. 2020), emcee (Foreman-Mackey et al. 2013), corner (Foreman-Mackey 2016)

APPENDIX
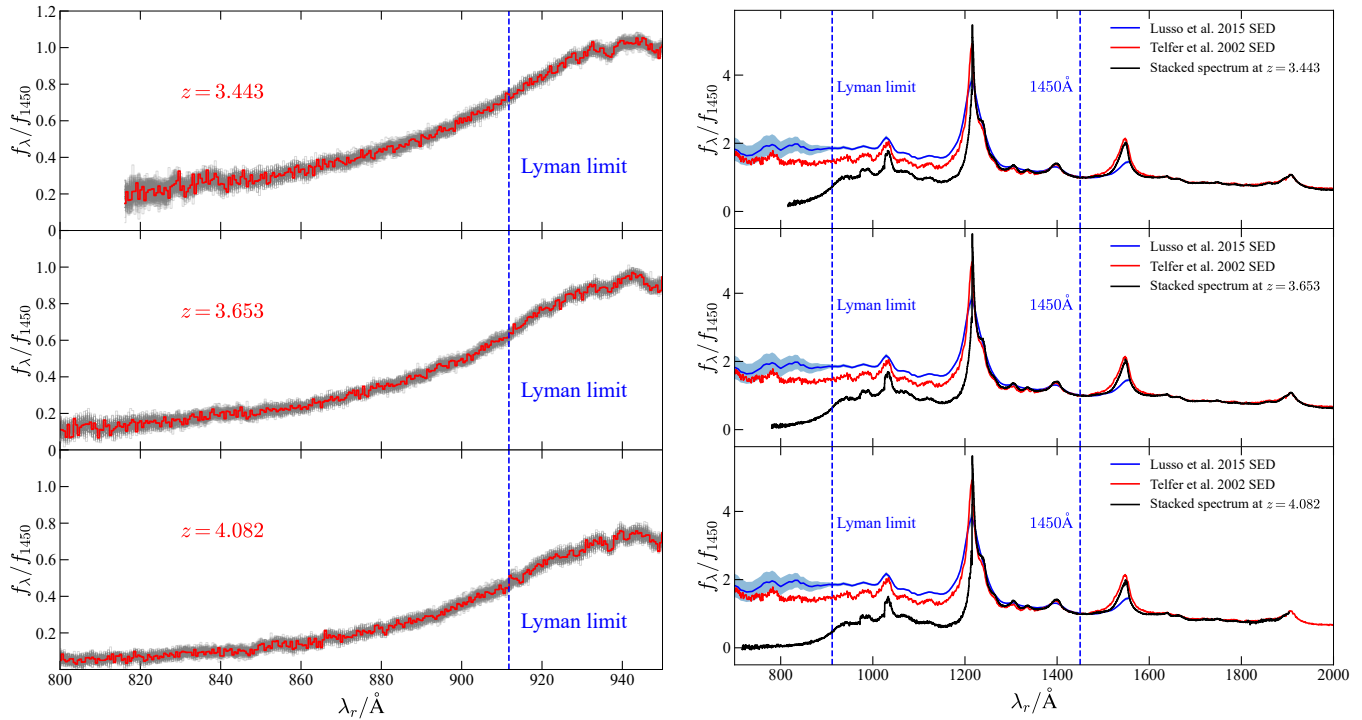
Figure 10. Left panel: Examples of the composite spectra from bootstrap technique (grey), together with the composite spectra from the normal stacking procedure (red). Right panel: Comparisons between the SED templates and our composite spectra at $700\text{Å} \leq \lambda_r \leq 2000\text{Å}$.

A. EXAMPLES OF SPECTRA

To better illustrate the uncertainty level of our composite spectra, we show examples of the bootstrap spectra in Figure 10. The redshift is chosen to be the same as Figure 2. We also show the spectra redward of Lymanα at the right panels of Figure 10 together with SED templates.

B. LYMAN SERIES OPACITY EVOLUTION

In Equation 4, we approximate the Lyman series opacity using a power law and the index γ_τ is chosen to be 3. Figure 11 shows the comparison between our $\gamma_\tau = 3$ approximation and the Lyman series opacity calculated with Prochaska et al. (2014) model, which shows only $\lesssim 1\%$ difference, indicating that $\gamma_\tau = 3$ is a suitable approximation.

C. PREVIOUS ESTIMATES OF $\lambda_{\mathrm{mfp}}^{912}$

We compare our results with the previous estimates that use the similar method to ours, listed in Table 3. We do not use the results from Gaikwad et al. (2023) and Bosman (2021), as their methods are significantly different from ours, which may introduce unknown biases. We also do not use other early works that first estimate $f(N_{\mathrm{H\,I}}, z)$ and calculate $\lambda_{\mathrm{mfp}}^{912}$ using Equation 14 (e.g. Rudie et al. 2013), as they suffer from biases such as line blending and absorber clustering (Prochaska et al. 2014).
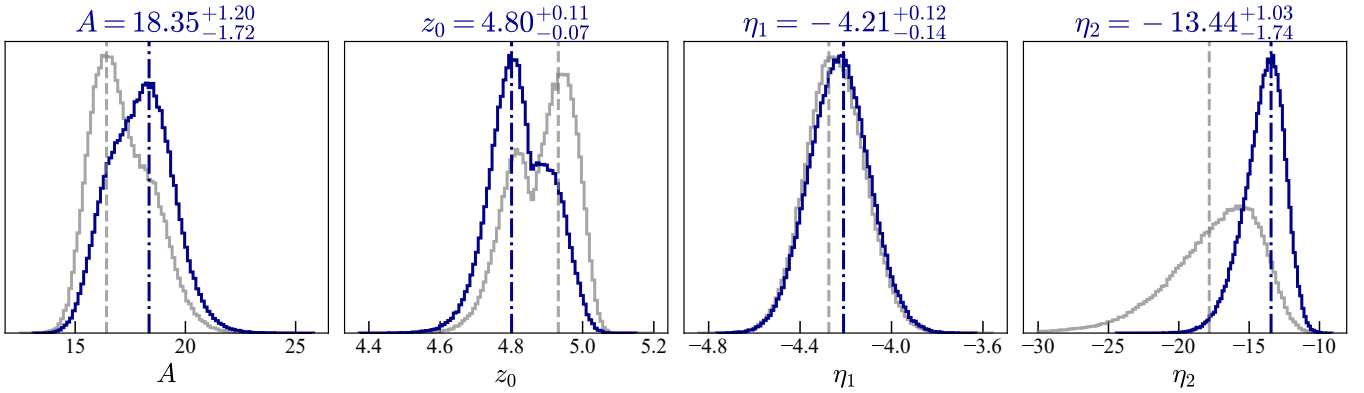
D. BROKEN POWER LAW FITTING WITH MORE DATA

In Section 4.3 we fit the broken power law model with the measurements in P09, O'Meara et al. (2013), Fumagalli et al. (2013), W14, Lusso et al. (2018), Becker et al. (2021), Zhu et al. (2023) and our results. In Gaikwad et al. (2023), Davies et al. (2024) and Satyavolu et al. (2024), the authors measured the $\lambda_{\mathrm{mfp}}^{912}$ at $5 \lesssim z \lesssim 6$ independently with various cosmological radiative transfer simulations. As their methods are mostly model-dependent and thus different from the direct method of others, we do not include their results in our fitting in Section 4.3. Here we present the broken power law fitting when incorporating them and show the MCMC parameter posterior in Figure 12 together with the posterior in Section 4.3. The two posteriors are mostly consistent, and biggest difference would be that the broken redshift is lowered to 4.8. Another interesting thing about the posterior of z_0 is that the implicit second peak at $z_0 \sim 4.8$ in the
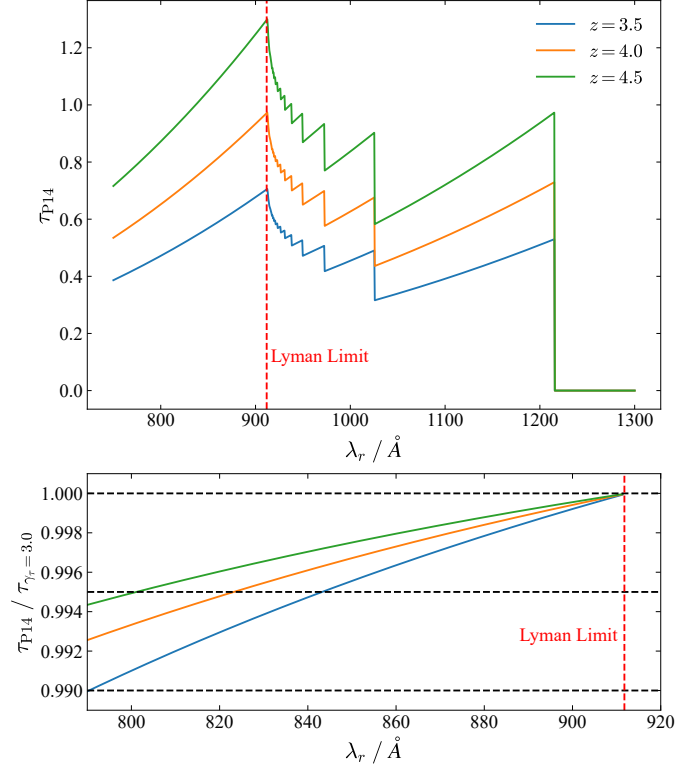
Figure 11. The Lyman series optical depth calculated using the $f(N_{\mathrm{H\,I}}, z)$ model in Prochaska et al. (2014) (P14), at the restframe of three $z = 3.5$ (blue), 4.0 (orange) and 4.5 (green) quasars. The upper panel shows the optical depth accounting for all Lyman series lines. The lower panel shows the ratio of the optical depth calculated from P14 model and our Equation 4, with the black horizontal dash lines representing 1.000, 0.995 and 0.990 and the red vertical dash line representing the Lyman limit wavelength (912Å). The Lyman series opacity at the blueward of the Lyman limit wavelength clearly evolves, and our approximation of Lyman series optical depth in Equation 4 is shown to produce only $< 1\%$ systematic error, and for most cases $< 0.5\%$.

Figure 12. Marginalized parameter posterior of broken power law fitting when incorporating data from Gaikwad et al. (2023), Davies et al. (2024) and Satyavolu et al. (2024). The blue histograms are the normalized posterior, the blue vertical dash-dot lines indicate the maximum posterior estimation, and the blue titles are the parameter estimations with the uncertainties defined in the way described in Section 4.3. For comparison, we also show the marginalized posterior from Section 4.3 in grey lines.

original posterior is strengthened and becomes the major peak after including more data, implying that the possibility of $z_0 = 4.80$ cannot be simply excluded and future data are still needed to distinguish the two cases.

Table 3. $\lambda_{\mathrm{mfp}}^{912}$ measurements from literature. The unit of $\lambda_{\mathrm{mfp}}^{912}$ is h_{70}^{-1} Mpc.

z_{qso}	N_{qso}	$\lambda_{\mathrm{mfp}}^{912}$	$\sigma\left(\lambda_{\mathrm{mfp}}^{912}\right)$	Reference
2.09	48	314.5	64.9	Lusso et al. (2018)
				(Low-z sample)
2.44	46	140.7	20.2	Lusso et al. (2018)
				(High-z sample)
2.44	53	235.8	40.3	O'Meara et al. (2013)
3.00	61	110.0	34	Fumagalli et al. (2013)
3.73	150	52.8	5.7	P09
3.78	150	45	4.2	P09
3.83	150	44.3	4.8	P09
3.88	150	46.5	4.8	P09
3.96	150	38.9	3.7	P09
4.07	150	33	3.5	P09
4.22	150	28.1	2.9	P09
4.56	57	22.2	2.3	W14
4.86	49	15.1	1.8	W14
5.16	39	10.3	1.6	W14
5.08	44	9.33	+2.06/-1.8	Zhu et al. (2023)
5.31	26	5.4	+1.47/-1.40	Zhu et al. (2023)
5.65	9	3.31	+2.74/-1.34	Zhu et al. (2023)
5.93	18	0.81	+0.73/-0.48	Zhu et al. (2023)
5.1	63	9.09	+1.62/-1.28	Becker et al. (2021)
6.0	13	0.75	+0.65/-0.45	Becker et al. (2021)

REFERENCES

Alexander, D. M., Davis, T. M., Chaussidon, E., et al. 2023, AJ, 165, 124, doi: 10.3847/1538-3881/acacfc

Anand, A., Guy, J., Bailey, S., et al. 2024, AJ, 168, 124, doi: 10.3847/1538-3881/ad60c2

Astropy Collaboration, Robitaille, T. P., Tollerud, E. J., et al. 2013, A&A, 558, A33, doi: 10.1051/0004-6361/201322068

Astropy Collaboration, Price-Whelan, A. M., Lim, P. L., et al. 2022, ApJ, 935, 167, doi: 10.3847/1538-4357/ac7c74

Bailey, S. J., et al. 2024, in prep.

Becker, G. D., & Bolton, J. S. 2013, MNRAS, 436, 1023, doi: 10.1093/mnras/stt1610

Becker, G. D., D'Aloisio, A., Christenson, H. M., et al. 2021, MNRAS, 508, 1853, doi: 10.1093/mnras/stab2696

Becker, G. D., Hewett, P. C., Worseck, G., & Prochaska, J. X. 2013, MNRAS, 430, 2067, doi: 10.1093/mnras/stt031

Bolton, J. S., & Haehnelt, M. G. 2007, MNRAS, 382, 325, doi: 10.1111/j.1365-2966.2007.12372.x

Bosman, S. E. I. 2021, arXiv e-prints, arXiv:2108.12446, doi: 10.48550/arXiv.2108.12446

Bosman, S. E. I., Davies, F. B., Becker, G. D., et al. 2022, MNRAS, 514, 55, doi: 10.1093/mnras/stac1046

Busca, N., & Balland, C. 2018, arXiv e-prints, arXiv:1808.09955, doi: 10.48550/arXiv.1808.09955

Cai, Z.-Y., & Wang, J.-X. 2023, Nature Astronomy, 7, 1506, doi: 10.1038/s41550-023-02088-5

Cain, C., D'Aloisio, A., Gangolli, N., & Becker, G. D. 2021, ApJL, 917, L37, doi: 10.3847/2041-8213/ac1ace

Cardelli, J. A., Clayton, G. C., & Mathis, J. S. 1989, ApJ, 345, 245, doi: 10.1086/167900

Chaussidon, E., Yèche, C., Palanque-Delabrouille, N., et al. 2023, ApJ, 944, 107, doi: 10.3847/1538-4357/acb3c2

Choudhury, T. R., Paranjape, A., & Bosman, S. E. I. 2021, MNRAS, 501, 5782, doi: 10.1093/mnras/stab045

Cowie, L. L., Barger, A. J., & Trouille, L. 2009, ApJ, 692, 1476, doi: 10.1088/0004-637X/692/2/1476

Davé, R., Anglés-Alcázar, D., Narayanan, D., et al. 2019, MNRAS, 486, 2827, doi: 10.1093/mnras/stz937

Davies, F. B., Bosman, S. E. I., Gaikwad, P., et al. 2024, ApJ, 965, 134, doi: 10.3847/1538-4357/ad1d5d

18

DESI Collaboration, Aghamousa, A., Aguilar, J., et al. 2016a, arXiv e-prints, arXiv:1611.00036, doi: 10.48550/arXiv.1611.00036

—. 2016b, arXiv e-prints, arXiv:1611.00037, doi: 10.48550/arXiv.1611.00037

DESI Collaboration, Abareshi, B., Aguilar, J., et al. 2022, AJ, 164, 207, doi: 10.3847/1538-3881/ac882b

DESI Collaboration, Adame, A. G., Aguilar, J., et al. 2024a, arXiv e-prints, arXiv:2404.03000, doi: 10.48550/arXiv.2404.03000

—. 2024b, arXiv e-prints, arXiv:2404.03001, doi: 10.48550/arXiv.2404.03001

—. 2024c, arXiv e-prints, arXiv:2404.03002, doi: 10.48550/arXiv.2404.03002

—. 2024d, AJ, 167, 62, doi: 10.3847/1538-3881/ad0b08

—. 2024e, AJ, 168, 58, doi: 10.3847/1538-3881/ad3217

DESI Collaboration, et al. 2025, in prep.

Dey, A., Schlegel, D. J., Lang, D., et al. 2019, AJ, 157, 168, doi: 10.3847/1538-3881/ab089d

Ding, J., Madau, P., & Prochaska, J. X. 2024, MNRAS, 532, 2082, doi: 10.1093/mnras/stae1510

Fan, X., Bañados, E., & Simcoe, R. A. 2023, ARA&A, 61, 373, doi: 10.1146/annurev-astro-052920-102455

Fan, X., Strauss, M. A., Becker, R. H., et al. 2006, AJ, 132, 117, doi: 10.1086/504836

Faucher-Giguère, C.-A. 2020, MNRAS, 493, 1614, doi: 10.1093/mnras/staa302

Faucher-Giguère, C.-A., Lidz, A., Hernquist, L., & Zaldarriaga, M. 2008a, ApJ, 688, 85, doi: 10.1086/592289

Faucher-Giguère, C.-A., Lidz, A., Zaldarriaga, M., & Hernquist, L. 2009, ApJ, 703, 1416, doi: 10.1088/0004-637X/703/2/1416

Faucher-Giguère, C.-A., Prochaska, J. X., Lidz, A., Hernquist, L., & Zaldarriaga, M. 2008b, ApJ, 681, 831, doi: 10.1086/588648

Filbert, S., Martini, P., Seebaluck, K., et al. 2024, MNRAS, 532, 3669, doi: 10.1093/mnras/stae1610

Foreman-Mackey, D. 2016, The Journal of Open Source Software, 1, 24, doi: 10.21105/joss.00024

Foreman-Mackey, D., Hogg, D. W., Lang, D., & Goodman, J. 2013, PASP, 125, 306, doi: 10.1086/670067

Fumagalli, M., O'Meara, J. M., Prochaska, J. X., & Worseck, G. 2013, ApJ, 775, 78, doi: 10.1088/0004-637X/775/1/78

Gaikwad, P., Srianand, R., Haehnelt, M. G., & Choudhury, T. R. 2021, MNRAS, 506, 4389, doi: 10.1093/mnras/stab2017

Gaikwad, P., Haehnelt, M. G., Davies, F. B., et al. 2023, MNRAS, 525, 4093, doi: 10.1093/mnras/stad2566

Gnedin, N. Y., & Madau, P. 2022, Living Reviews in Computational Astrophysics, 8, 3, doi: 10.1007/s41115-022-00015-5

Greig, B., Mesinger, A., Bañados, E., et al. 2024, MNRAS, 530, 3208, doi: 10.1093/mnras/stae1080

Gunn, J. E., & Peterson, B. A. 1965, ApJ, 142, 1633, doi: 10.1086/148444

Guy, J., Bailey, S., Kremin, A., et al. 2023, AJ, 165, 144, doi: 10.3847/1538-3881/acb212

Haardt, F., & Madau, P. 1996, ApJ, 461, 20, doi: 10.1086/177035

—. 2012, ApJ, 746, 125, doi: 10.1088/0004-637X/746/2/125

Hall, P. B., Anderson, S. F., Strauss, M. A., et al. 2002, ApJS, 141, 267, doi: 10.1086/340546

Hunter, J. D. 2007, Computing in Science and Engineering, 9, 90, doi: 10.1109/MCSE.2007.55

Inoue, A. K., Shimizu, I., Iwata, I., & Tanaka, M. 2014, MNRAS, 442, 1805, doi: 10.1093/mnras/stu936

Jiang, L., Ning, Y., Fan, X., et al. 2022, Nature Astronomy, 6, 850, doi: 10.1038/s41550-022-01708-w

Jin, X., Yang, J., Fan, X., et al. 2023, ApJ, 942, 59, doi: 10.3847/1538-4357/aca678

Kamble, V., Dawson, K., du Mas des Bourboux, H., Bautista, J., & Scheinder, D. P. 2020, ApJ, 892, 70, doi: 10.3847/1538-4357/ab76bd

Koposov, S. E., Allende Prieto, C., Cooper, A. P., et al. 2024, MNRAS, 533, 1012, doi: 10.1093/mnras/stae1842

Kulkarni, G., Keating, L. C., Haehnelt, M. G., et al. 2019, MNRAS, 485, L24, doi: 10.1093/mnrasl/slz025

Lewis, J. S. W., Ocvirk, P., Sorce, J. G., et al. 2022, MNRAS, 516, 3389, doi: 10.1093/mnras/stac2383

Lusso, E., Fumagalli, M., Rafelski, M., et al. 2018, ApJ, 860, 41, doi: 10.3847/1538-4357/aac514

Lusso, E., Worseck, G., Hennawi, J. F., et al. 2015, MNRAS, 449, 4204, doi: 10.1093/mnras/stv516

Madau, P. 2017, ApJ, 851, 50, doi: 10.3847/1538-4357/aa9715

Madau, P., & Haardt, F. 2015, ApJL, 813, L8, doi: 10.1088/2041-8205/813/1/L8

McGreer, I. D., Mesinger, A., & D'Odorico, V. 2015, MNRAS, 447, 499, doi: 10.1093/mnras/stu2449

Meiksin, A., & Madau, P. 1993, ApJ, 412, 34, doi: 10.1086/172898

O'Meara, J. M., Prochaska, J. X., Worseck, G., Chen, H.-W., & Madau, P. 2013, ApJ, 765, 137, doi: 10.1088/0004-637X/765/2/137

Oppenheimer, B. D., & Davé, R. 2006, MNRAS, 373, 1265, doi: 10.1111/j.1365-2966.2006.10989.x

Planck Collaboration, Aghanim, N., Akrami, Y., et al. 2021, A&A, 652, C4, doi: 10.1051/0004-6361/201833910e

Prochaska, J. X., Madau, P., O'Meara, J. M., & Fumagalli, M. 2014, MNRAS, 438, 476, doi: 10.1093/mnras/stt2218

Prochaska, J. X., O'Meara, J. M., & Worseck, G. 2010, ApJ, 718, 392, doi: 10.1088/0004-637X/718/1/392

Prochaska, J. X., Worseck, G., & O'Meara, J. M. 2009, ApJL, 705, L113, doi: 10.1088/0004-637X/705/2/L113

Puchwein, E., Haardt, F., Haehnelt, M. G., & Madau, P. 2019, MNRAS, 485, 47, doi: 10.1093/mnras/stz222

Rauch, M. 1998, ARA&A, 36, 267, doi: 10.1146/annurev.astro.36.1.267

Romano, M., Grazian, A., Giallongo, E., et al. 2019, A&A, 632, A45, doi: 10.1051/0004-6361/201935550

Roth, J. T., D'Aloisio, A., Cain, C., et al. 2024, MNRAS, 530, 5209, doi: 10.1093/mnras/stae1194

Rudie, G. C., Steidel, C. C., Shapley, A. E., & Pettini, M. 2013, ApJ, 769, 146, doi: 10.1088/0004-637X/769/2/146

Satyavolu, S., Kulkarni, G., Keating, L. C., & Haehnelt, M. G. 2024, MNRAS, 533, 676, doi: 10.1093/mnras/stae1717

Schaye, J., Crain, R. A., Bower, R. G., et al. 2015, MNRAS, 446, 521, doi: 10.1093/mnras/stu2058

Schlafly, E. F., Kirkby, D., Schlegel, D. J., et al. 2023, AJ, 166, 259, doi: 10.3847/1538-3881/ad0832

Schlegel, D. J., Finkbeiner, D. P., & Davis, M. 1998, ApJ, 500, 525, doi: 10.1086/305772

Schneider, D. P., Richards, G. T., Hall, P. B., et al. 2010, AJ, 139, 2360, doi: 10.1088/0004-6256/139/6/2360

Somerville, R. S., & Davé, R. 2015, ARA&A, 53, 51, doi: 10.1146/annurev-astro-082812-140951

Songaila, A., & Cowie, L. L. 2010, ApJ, 721, 1448, doi: 10.1088/0004-637X/721/2/1448

Spina, B., Bosman, S. E. I., Davies, F. B., Gaikwad, P., & Zhu, Y. 2024, A&A, 688, L26, doi: 10.1051/0004-6361/202450798

Stevans, M. L., Shull, J. M., Danforth, C. W., & Tilton, E. M. 2014, ApJ, 794, 75, doi: 10.1088/0004-637X/794/1/75

Telfer, R. C., Zheng, W., Kriss, G. A., & Davidsen, A. F. 2002, ApJ, 565, 773, doi: 10.1086/324689

Turner, W., Martini, P., Göksel Karaçaylı, N., et al. 2024, arXiv e-prints, arXiv:2405.06743, doi: 10.48550/arXiv.2405.06743

van der Walt, S., Colbert, S. C., & Varoquaux, G. 2011, Computing in Science and Engineering, 13, 22, doi: 10.1109/MCSE.2011.37

Ďurovčíková, D., Eilers, A.-C., Chen, H., et al. 2024, ApJ, 969, 162, doi: 10.3847/1538-4357/ad4888

Villasenor, B., Robertson, B., Madau, P., & Schneider, E. 2021, ApJ, 912, 138, doi: 10.3847/1538-4357/abed5a

Virtanen, P., Gommers, R., Oliphant, T. E., et al. 2020, Nature Methods, 17, 261, doi: 10.1038/s41592-019-0686-2

Weymann, R. J., Morris, S. L., Foltz, C. B., & Hewett, P. C. 1991, ApJ, 373, 23, doi: 10.1086/170020

Worseck, G., & Prochaska, J. X. 2011, ApJ, 728, 23, doi: 10.1088/0004-637X/728/1/23

Worseck, G., Prochaska, J. X., O'Meara, J. M., et al. 2014, MNRAS, 445, 1745, doi: 10.1093/mnras/stu1827

Yang, J., Wang, F., Fan, X., et al. 2020, ApJ, 904, 26, doi: 10.3847/1538-4357/abbc1b

Zhu, Y., Becker, G. D., Bosman, S. E. I., et al. 2021, ApJ, 923, 223, doi: 10.3847/1538-4357/ac26c2

—. 2022, ApJ, 932, 76, doi: 10.3847/1538-4357/ac6e60

Zhu, Y., Becker, G. D., Christenson, H. M., et al. 2023, ApJ, 955, 115, doi: 10.3847/1538-4357/aceef4

Zhu, Y., Becker, G. D., Bosman, S. E. I., et al. 2024, MNRAS, 533, L49, doi: 10.1093/mnrasl/slae061